Application of a data-driven simulation method to the reconstruction of the coronal magnetic field [*]

Yu-Liang Fan, Hua-Ning Wang, Han He and Xiao-Shuai Zhu

Key Laboratory of Solar Activity, National Astronomical Observatories, Chinese Academy of Sciences, Beijing 100012, China; *fanyuliang@bao.ac.cn*

Abstract Ever since the magnetohydrodynamic (MHD) method for extrapolation of the solar coronal magnetic field was first developed to study the dynamic evolution of twisted magnetic flux tubes, it has proven to be efficient in the reconstruction of the solar coronal magnetic field. A recent example is the so-called data-driven simulation method (DDSM), which has been demonstrated to be valid by an application to model analytic solutions such as a force-free equilibrium given by Low and Lou. We use DDSM for the observed magnetograms to reconstruct the magnetic field above an active region. To avoid an unnecessary sensitivity to boundary conditions, we use a classical total variation diminishing Lax-Friedrichs formulation to iteratively compute the full MHD equations. In order to incorporate a magnetogram consistently and stably, the bottom boundary conditions are derived from the characteristic method. In our simulation, we change the tangential fields continually from an initial potential field to the vector magnetogram. In the relaxation, the initial potential field is changed to a nonlinear magnetic field until the MHD equilibrium state is reached. Such a stable equilibrium is expected to be able to represent the solar atmosphere at a specified time. By inputting the magnetograms before and after the X3.4 flare that occurred on 2006 December 13, we find a topological change after comparing the magnetic field before and after the flare. Some discussions are given regarding the change of magnetic configuration and current distribution. Furthermore, we compare the reconstructed field line configuration with the coronal loop observations by XRT onboard *Hinode*. The comparison shows a relatively good correlation.

Key words: Sun: activity — Sun: flares — Sun: corona

1 INTRODUCTION

The knowledge of a 3D coronal magnetic field is crucial in the understanding of a wide range of active phenomena in the solar atmosphere. The coronal magnetic field can be described with equations

$$\nabla \times \boldsymbol{B} = \alpha \boldsymbol{B}, \qquad \nabla \cdot \boldsymbol{B} = 0, \tag{1}$$

where α is called the force-free factor. If $\alpha = 0$ or a constant these equations describe a potential or linear force-free field, and furthermore $\alpha \neq \mathrm{constant}$ indicates a nonlinear force-free field (NLFFF).

The NLFFF is believed to exist close to magnetic fields in the corona with low beta. Several methods for the NLFFF extrapolation were proposed, such as the optimization methods (Wheatland et al. 2000; Wiegelmann 2004), boundary integral methods (Yan & Sakurai 2000; He & Wang 2008), and Grad-Rubin-like methods (Régnier & Amari 2004). However, the force-free field is just an approximation with gravity and plasma pressure ignored in the solar atmosphere. In order to take account of the non-linear interactions between the plasma flow field and magnetic field, it is necessary to invoke full magnetohydrodynamic (MHD) equations for the coronal magnetic field reconstruction.

The first model invoking full MHD equations was developed by Mikic et al. (1990) to study the dynamic evolution of twisted magnetic flux tubes. McClymont & Mikic (1994) solved a subset of the full MHD equations to derive horizontal photospheric flows, using physical quantities deduced from the observed magnetogram as the initial conditions. Roumeliotis (1996) introduced a similarly evolutionary method, named the "stress-and-relax method," which iteratively evolves the initial potential field by stressing and relaxing phases into a non-linear nearly force-free field until the bottom transverse field matches the magnetogram. Valori et al. (2005) devised a magnetofrictional method based on the stress-and-relax method.

Recently, a more robust simulation implemented by the space-time conservation element and solution element (CESE) method has been validated to reconstruct the magnetic field of Low & Lou (1990)'s test cases (Jiang et al. 2011). In Jiang et al.'s model, the lower boundary magnetic fields are extracted from Low & Lou (1990)'s field model as the driven force. On the bottom boundary condition, Jiang et al. fixed the density and pressure, and set the velocity equal to zero all the time for the sake of stability.

Although the CESE method has proved to be effective in the reconstruction of Low & Lou's test case, the problem is that the CESE method is sensitive to noise in the boundary conditions, which is the main reason to fix the induced plasma velocity to zero on the bottom. In the case of reconstruction of Low & Lou's analytical magnetic fields, there is little noise in the boundary conditions to cause numerical instability. When observed magnetograms are taken as the boundary conditions for Jiang et al.'s model, the observational data cause computational instability unless an enhanced smoothness is applied to these magnetograms. In order to overcome difficulties in Jiang et al.'s model, we suggest a relatively simple total variance diminishing (TVD) solver, which allows noise in the boundary conditions, and uses a characteristic boundary treatment where density, pressure and velocity are not fixed.

Since the extrapolated field configuration strongly depends on the implementation of boundary conditions, we employ the data-driven simulation method (DDSM), in which boundary conditions are derived from the projected normal characteristic method (Wu et al. 2006). The advantage of this method is that the temporal evolution of MHD variables on the sub-Alfvénic boundary will match both the governing MHD equations and the given boundary conditions (Hayashi 2005). It is important to note that the boundary conditions are crucial to the simulation results. Simple boundary conditions obtained with linear extrapolation lead to the numerical instability, while boundary conditions produced with the projected normal characteristic method lead to the numerical stability (Nakagawa et al. 1987). Since the characteristic method allows us to incorporate components of observed magnetograms as a part of the lower boundary condition in a more natural way (Wang et al. 2008a), these magnetograms can be taken as the driving source in our simulation. DDSM has been implemented to study the evolution of Poynting flux in active regions (Fan et al. 2011). In Fan et al.'s model, they used the velocity distributions generated by DDSM to compute physical parameters like the Poynting flux.

In order to describe the DDSM and show an example of application to extrapolation, this paper is organized as follows: in Section 2, the DDSM and its numerical implementation are briefly introduced; in Section 3, this method is applied to NOAA 10930, and some analysis and comparisons are presented. Finally, discussion and conclusions are given in Section 4.

2 DATA AND METHOD

We solve the three-dimensional resistive and compressible MHD equations in Cartesian coordinates, and ignore the effects of radiative cooling, heat conduction and those of higher order transport such as differential rotation and meridional flow. The equations can be written in their primitive forms as follows:

$$\frac{\partial \rho}{\partial t} + \nabla \cdot (\rho \boldsymbol{v}) = 0, \tag{2}$$

$$\rho\left(\frac{\partial \boldsymbol{v}}{\partial t} + \boldsymbol{v} \cdot \nabla \boldsymbol{v}\right) = -\nabla p + \frac{1}{4\pi} (\nabla \times \boldsymbol{B}) \times \boldsymbol{B} + \rho g, \tag{3}$$

$$\frac{\partial p}{\partial t} + \boldsymbol{v} \cdot \nabla p + \gamma p \nabla \cdot \boldsymbol{v} = (\gamma - 1)\eta \boldsymbol{J^2}, \tag{4}$$

$$\frac{\partial \boldsymbol{B}}{\partial t} = \nabla \times (\boldsymbol{v} \times \boldsymbol{B}) + \eta \nabla^2 \boldsymbol{B}, \tag{5}$$

where $\boldsymbol{J}$ is the electric current, γ is the specific heat ratio and η is the coefficient of diffusion.

Concerning the magnetic field configuration in the higher corona, the specific heat ratio γ is chosen to be 1.05 and the magnetic diffusivity η is chosen to be 0.01. The normalization of typical values describing parameters in the corona is given in Table 1.

The initial condition of DDSM can be set as follows: the initial trial density is set to be uniform at the bottom and decreases exponentially with the scale height to account for the solar gravity; the initial magnetic field is set to be a potential field extrapolated from the line-of-sight component of the vector magnetogram by using the Green's function method (Metcalf et al. 2006); the initial velocity is set equal to zero everywhere and the temperature is set to be uniform.

In the DDSM simulation, normal components of the magnetic field are unchanged on the boundary, but tangential components are continually changed when the initial potential field evolves to the observed field. During the evolution of magnetic fields at the bottom, the Lorentz forces are continuously injected into the computational domain. The injected forces cause the initial potential fields to change to nonlinear fields during the relaxation process until the MHD equilibrium state is reached. It takes tens of Alfvén times to reach this equilibrium state which should be able to represent the solar atmosphere at a specified time. As the forces are re-balanced during the relaxation process, a stable equilibrium is expected, in which the force-free status appears only when the pressure is counteracted by gravity (Aschwanden 2004).

In order to stay numerically stable, a classical total variation diminishing (TVD) Lax-Friedrichs formulation was employed to iteratively compute the full MHD equations, which is a relatively simple TVD type scheme that enables us to compute data with large noise. We use a TVDLF solver to solve the MHD equations implemented in the Versatile Advection Code (VAC) by Tóth (1996), which is a software package for solving hydrodynamic and MHD problems in astrophysics.

Table 1 Units for Normalization

Quantity	Value
g	10^4 cm s^{-2}
n	10^9 cm^{-3}
T	10^6 K
L	100 Mm
v	100 km s^{-1}
t	10^3 s
B	0.5 G

Notes: g is gravitational acceleration, n is number density, T is temperature, L is pressure scale height, v is Alfvén speed, t is Alfvén crossing time, and B is magnetic field strength.

The boundary condition is also a source of instability when it is treated inappropriately. We choose the lower physical boundary condition to be derived with projected characteristics (Nakagawa 1981a,b; Nakagawa et al. 1987), which eigen-decomposes the hyperbolic system into a set of compatible equations corresponding to a set of wave modes. According to the projected characteristics, the outgoing MHD waves are used to compute variables on the boundary and the incoming waves are abandoned. We can add constraints obtained from observed magnetograms to make up for the absence of the incoming wave. In this way, we consistently incorporate the magnetogram as part of the bottom boundary condition.

The advantage of using the projected characteristics is that the temporal evolution of MHD variables on the sub-Alfvénic boundary will match both the governing MHD equations and the given boundary conditions (Hayashi 2005; Wu et al. 2006). The density and pressure on the boundary need not remain unchanged and the velocity need not be set to zero. Another advantage is that the boundary conditions produced with the characteristic method make the simulation running over a long time very stable. The detailed numerical implementation and derived expressions describing the time-varying physical parameters on the boundary are given in the Appendix of Wu et al. (2006).

We choose magnetograms from the active region NOAA 10930 observed by *Hinode* to be the boundary condition in our simulation. This active region was reported in an X3.4 flare on 2006 December 13. Observations show that before the flare there was a significant flux emergence between the positive and negative sunspots. Vector magnetograms are derived through the inversion of Stokes profiles with a Milne-Eddington atmosphere (Lites et al. 1993), using the full polarization parameters (*I, Q, U,* and *V*) from the SOT/SP. The $180°$ ambiguity in the vector magnetogram is resolved by using the minimum energy algorithm by Metcalf (1994), which uses simulated annealing to minimize both the electric current density and the field divergence. The magnetograms are also centered on the solar disk to remove the effect of projection.

The model is built in a 3D rectangular box in Cartesian coordinates with $100 \times 100 \times 70$ grids in the x, y, and z directions, respectively. The magnetogram is cropped to be a 50×50 grid which is embedded in the 100×100 computational domain. The pixel size of the magnetogram for the bottom condition is 2.56 arcsec. The main reason for that is to reduce the boundary effect since we set the boundary aside from the computational domain as much as possible.

3 RESULTS AND ANALYSIS

We apply DDSM to reconstruct the magnetic field of active region NOAA 10930 before and after an X3.4 flare, and take the observed magnetic field in Hinode/SP vector magnetograms as boundary conditions. In the relaxation, iterative computations are required to evolve the physical state governed by MHD equations, which is time consuming and resource intensive. When an equilibrium state is reached, the averaged plasma velocity becomes stationary, which could be a good sign that no more forces are generated. For this reason, we take the averaged plasma velocity, v_{avg}, in the computational volume with N grid points, $v_{\mathrm{avg}} = \frac{1}{N} \sum_i |v_i|$, as the indication of the equilibrium state. The evolution of v_{avg} is shown in the left panel of Figure 1. At the beginning of the computation, the velocity is set to zero. In order to make the initial potential field evolve slowly to reach the state of the observed field, increments of the initial field are set as small as possible, which results in the physical state governed by MHD equations evolving slowly. For this reason, the averaged velocity linearly increases in the driven phase, and becomes stationary in the relaxation phase after the computational tangential components have matched the observational ones.

For internal consistency of the reconstructed field, we also check the error of the divergence-free constraint. To have a quantitative understanding of how the error evolves in the simulation, we present a simple average of the summed error, $E_{\mathbf{d}}$, in the entire volume, V,

$$E_{\mathbf{d}} = \frac{1}{V} \sum_V |\nabla \cdot \boldsymbol{B}| \mathrm{d}V. \tag{6}$$
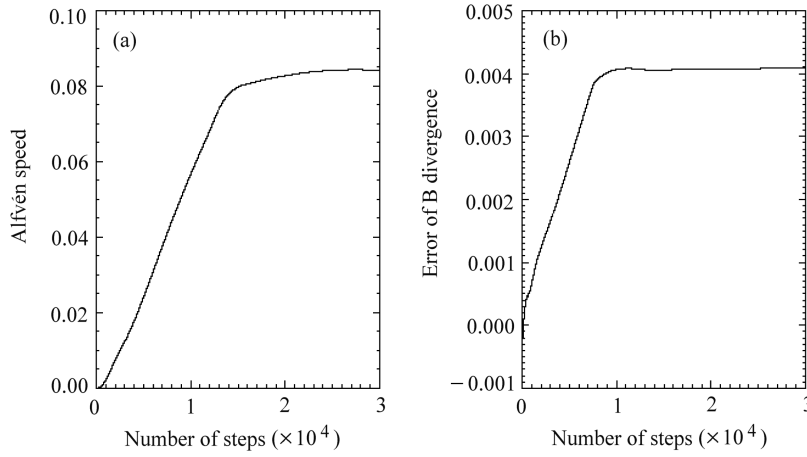
Fig. 1 (a) Time evolution of averaged velocity in the DDSM simulation. (b) The time evolution of the summed error of the divergence-free constraint in the DDSM simulation. The first 1×10^4 steps of DDSM are in the driven phase, but the latter 2×10^4 steps are in the relaxation phase. The averaged velocity is scaled in terms of Alfvén speed.
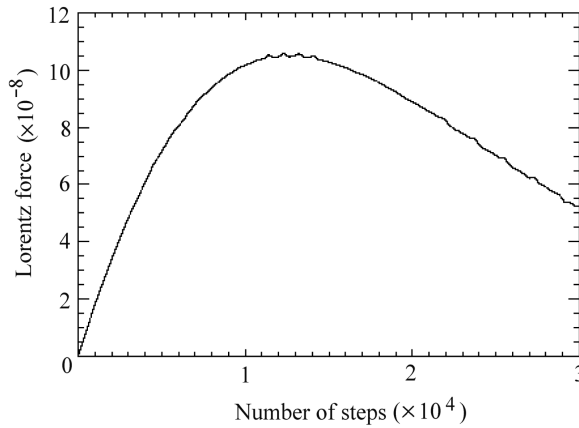

Fig. 2 Time evolution of averaged $J \times B$ in the DDSM simulation. The first 1×10^4 steps of DDSM are in the driven phase, but the latter 2×10^4 steps are in the relaxation phase. J and B are normalized in the unit of typical coronal values.

The evolution of $E_{\mathbf{d}}$ in the computational volume (Fig. 1(b)) behaves similarly to that of v_{avg}. In the driven phase, the tangential components of the initial potential field are changed to match those in the observational field (in the first 1×10^4 steps), causing the value of $E_{\mathbf{d}}$ to continuously climb to 0.004 and become stable in the relaxation phase, which means that the divergence error stops being injected into the volume. We also check the evolution of averaged $J \times B$ as shown in Figure 2, which represents the direction defined by the cross-product of J and B representing the bulk of the field lines. In the first 1×10^4 steps, the evolution of averaged $J \times B$ acts similarly to that of the divergence error. However, in the later relaxation phase, the averaged $J \times B$ decreases as time
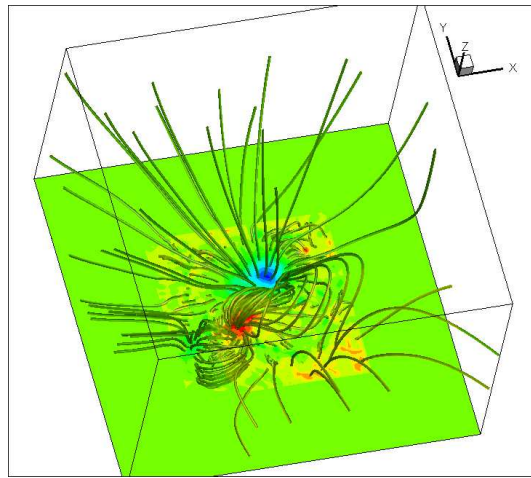
Fig. 3 Shown is the perspective view of the extrapolated magnetic fields obtained after the relaxation phase. The data we use for this extrapolation are chosen to be the magnetogram observed from 04:45–05:15 UT on 2006 December 13 after the X3.4 flare.
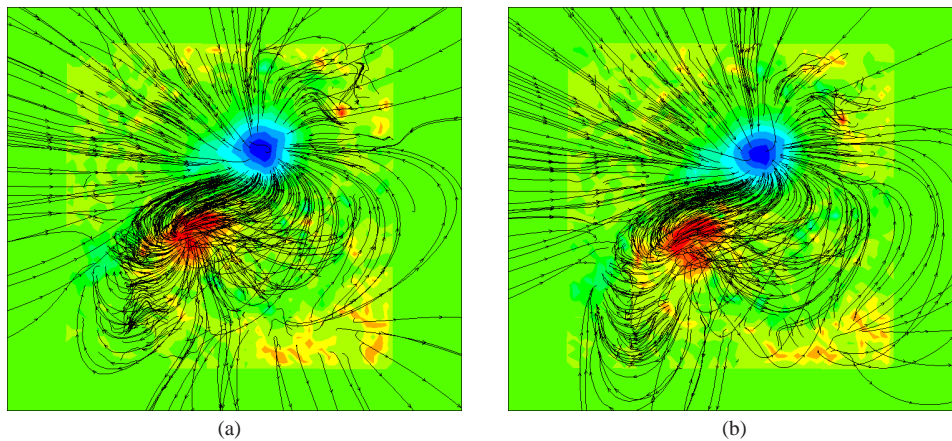

(a)   (b)

Fig. 4 Comparison of the topological and geometrical changes of the magnetic fields before and after the flare. *Left*: Extrapolated fields using the magnetogram from 20:45–21:15 UT on 2006 December 12 before the X3.4 flare. *Right*: Extrapolated result using the magnetogram from 04:45–05:15 UT on 2006 December 13 after the X3.4 flare.

goes on. This fact is easy to understand, because the numerical viscosity introduced by the algorithm relaxes the magnetic field system and continuously reduces the value of $\boldsymbol{J} \times \boldsymbol{B}$.

The extrapolated magnetic field could be obtained after the relaxation phase, and the perspective view of the resulting field is shown in Figure 3. We embed the original magnetogram into a large outer area where there is no magnetic field. The reason to do this is to avoid the side boundary reflection effect, which may generate unstable disturbances. The positive polarities are in red and the negative ones are in blue. The extrapolated magnetic field in Figure 3 is based on a magnetogram

observed during 20:45–21:15 UT on 2006 December 12 before the X3.4 flare. The observed magnetogram is cropped from the Fast Map mode of SP with pixel number 1000×512. Due to limited computational resources, the cropped magnetogram is rebinned to a 50×50 grid and embedded in the 100×100 grid.

In order to reveal the topological and geometrical changes of magnetic fields before and after the flare, we compare the results in Figure 4. Figure 4(a) is at pre-flare time and Figure 4(b) is at post-flare time. As we can see from the figure, the main changes reside in the low lying highly sheared closed loops. Magnetic fields across the polarity inversion line are highly sheared and twisted, but the interconnecting fields are less stressed after the flare. Also, in the eastern area surrounding the positive sunspot, the arched magnetic fields tend to have more potential and become higher after the flare. Besides, some of the low lying twisted loops even disappear, which is easily observed due to the relatively simple magnetic structure. From the resulting magnetic fields, we compute the magnetic energy to be 7.9×10^{32} erg before the flare and 7.5×10^{32} erg after the flare, with about a 5% drop in the magnetic energy.

Another way to examine the difference is to investigate the distribution of the current density. Since a current sheet can be an ideal place for instabilities (e.g. reconnection) to happen, and it can be the energy source for flares and CMEs, current density plays an important role in the study of solar dynamics. We compute the vector norm of the electric current densities before and after the flare and compare them to each other in Figure 5. The background is the gray scale contour of the longitudinal magnetogram, and the strongest current densities are plotted in red near the photosphere. It can be clearly recognized that before the flare the currents are distributed continuously along the polarity inversion lines. The current stripes connect the main sunspot groups, and run over the emerging flux regions. After the flare, the current stripes become fragmented and dispersed. Since compact currents are closely associated with the free energy in excess of the potential field (Schrijver et al. 2008), it is easy to understand the weakening of the current stripes as the flare and the associated CME tap energy from the current system.

In addition to the bottom distribution of the norm of current densities, we can also consider the 3D structures of the current densities above the polarity inversion line and area of emerging flux. Shown in Figure 6 is the 3D visualization of current density. Figure 6(a) is the side view of the 3D structure, and Figure 6(b) is the top view. The current system between opposite polarities can be decomposed into two parts: the low-lying compact current system and high-arching current system (Wang et al. 2008b; Schrijver et al. 2008). The low-lying current system is more dense and thus shown in a dark color, which follows the direction of the polarity inversion lines. The high-lying current system wraps around the low-lying currents and magnetic fields, and connects the opposite polarities. Following the idea of Schrijver et al. (2008), the low-lying current system can be seen as the consequence of emerging flux that carries the currents from the sub-photosphere region, so where the flux emergence is strong, the low-lying current is also strong. Since the high-lying current system is the result of the force-free condition that requires the current to be parallel to the direction of magnetic fields (Wang et al. 2008b), we can see highly arched currents running along the magnetic field in Figure 6.

It is interesting to note that there exist dips in the pre-flare field as shown in Figure 7(a). Those features cannot be found after the explosion, when the magnetic fields become less twisted and arch higher. The magnetic dips could trap dense prominence materials and be able to support a filament, which had been observed by the Paris-Meudon observatory using the Hα spectroheliograph (Guo et al. 2008).

Finally, we compare the reconstructed field line configuration with the XRT coronal loop observations shown in Figure 8(b). The magnetogram is observed on 2006 December 12 (20:45–21:15 UT) and the XRT image is chosen at 21:05 UT on 2006 December 12. From the comparison, we see that the field lines of the reconstructed fields generally agree with the coronal loop structures in the central region of NOAA 10930. As in the figure, the open field areas generally correspond
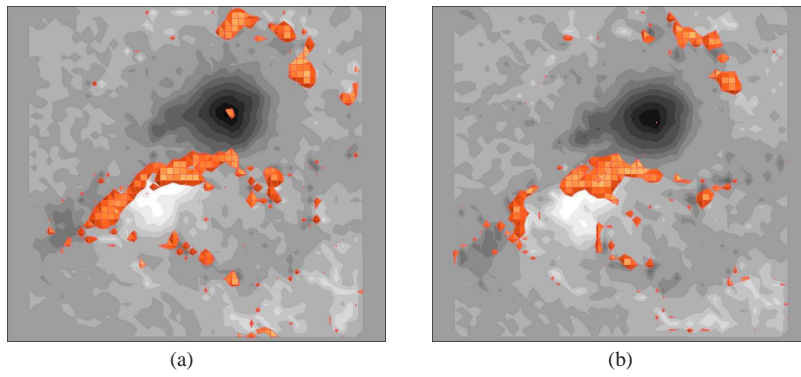
Fig. 5 Comparison of the distribution of the electric current density before and after the flare. (a) Computed result using the magnetogram from 20:45–21:15 UT on 2006 December 12 before the X3.4 flare. (b) Computed result using the magnetogram from 04:45–05:15 UT on 2006 December 13 after the X3.4 flare.
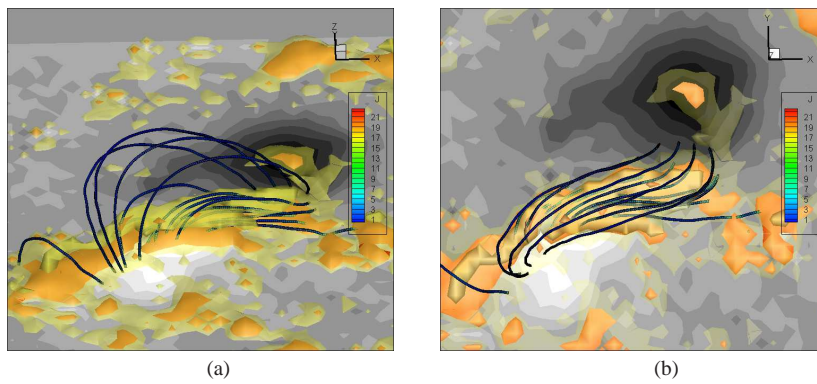

Fig. 6 3D structures of the current densities above the polarity inversion line from 20:45–21:15 UT on 2006 December 12 before the X3.4 flare. (a) a side view, (b) a top view.
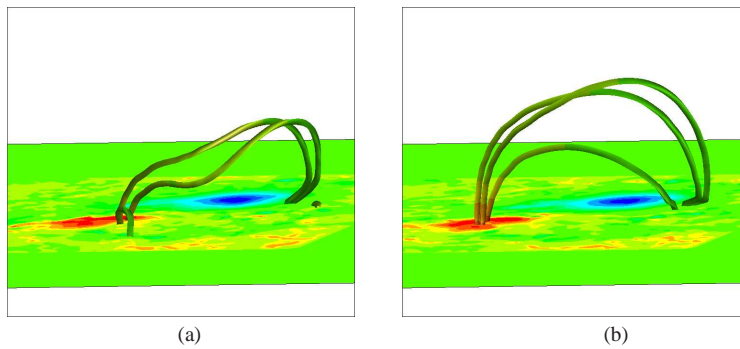

Fig. 7 (a) Dip structures using the magnetogram from 20:45–21:15 UT on 2006 December 12 before the X3.4 flare. (b) Post dip structures using the magnetogram from 20:45–21:15 UT for 04:45–05:15 UT on 2006 December 13 after the flare.
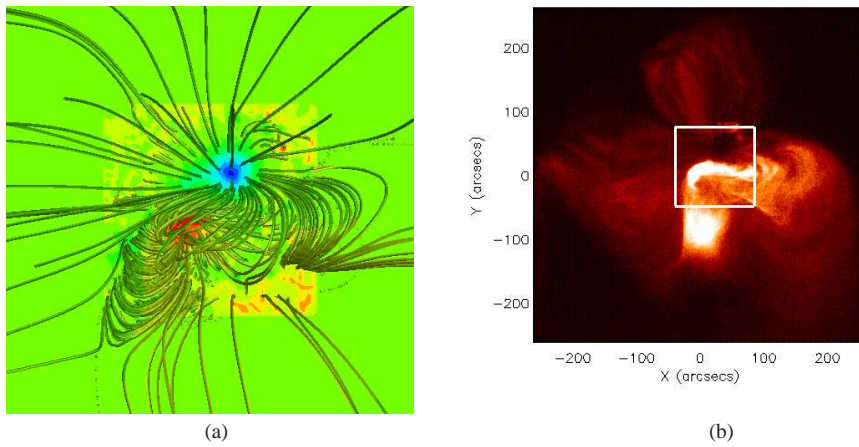
(a)   (b)

Fig. 8 (a) The extrapolation of the magnetogram from 20:45–21:15 UT on 2006 December 12 before the X3.4 flare. (b) The XRT image observed at 21:05 UT on 2006 December 12 before the X3.4 flare. The magnetogram used for the extrapolation corresponds to the white square box in the XRT image.

to the dark regions of the XRT image, but the closed field areas coincide with bright coronal loop regions. The extrapolated fields can be divided into two kinds of configurations: the low lying fields and the high arching fields. The low lying fields are highly sheared fields that correspond to dense structures in the XRT image. These field lines are nearly parallel to the polarity inversion lines. The high arching fields stretch into the corona, ranging from 2×10^4 km to 10×10^4 km, and have more potential than the low lying fields.

4 DISCUSSION AND CONCLUSIONS

In the current work, we use DDSM to reconstruct magnetic fields based on observed magnetograms. In the simulation with DDSM, tangential components of initial potential fields continually evolve to those in observed fields, and then these initial potential fields change into nonlinear fields when the MHD equilibrium state is reached. We choose a relatively simple TVD solver that allows larger noise on the boundary. This solver is easy to compute and requires little computational time. We also use the characteristic method to handle the bottom boundary. The characteristic boundary treatment produces stable numerical results, which are very useful for long running simulations. Furthermore, interactions between governing MHD equations and given boundary conditions can be taken into account, which means that parameters of density, pressure and velocity need not be fixed. It is more physically realistic to let variables on the boundary change according to the MHD equations.

We apply our scheme to Hinode/SP vector magnetograms observed from NOAA 10930 on 2006 December 12 (20:45–21:15 UT) and December 13 (04:45–05:15 UT) to reconstruct magnetic fields before and after the X3.4 flare, and compare their differences in terms of the flare and associated CME. Some quantities and properties (e.g. distribution of current densities, 3D fields and current density structures) are examined to facilitate our understanding of magnetic field line evolution. Finally, the extrapolated magnetic fields are compared to the coronal loop images obtained by the XRT onboard *Hinode*, and both of them have relatively good correlation.

It is important to note that the final equilibrium state is dynamic, and the generated steady state flows are necessary to drive the model magnetic field to compensate for dissipative effects from the imposed magnetic diffusivity. Since the imposed magnetic diffusivity is not dissipative enough,

there should be some electric currents in the final steady state situation. In this sense, the final dynamic equilibrium state is dependent on the corona's initial setting. If a different initial magnetic configuration is used (e.g., a nonlinear force free field instead of a potential one), the final steady state field should be different. We choose a potential field here because it is more consistent to drive potential fields to non-potential ones. If the nonlinear force free field is taken as the initial conditions for the time-dependent model, serial observed fields can be employed to drive the evolution.

References

Aschwanden, M. J. 2004, Physics of the Solar Corona. An Introduction, ed. Aschwanden, M. J. (Praxis Publishing Ltd)

Fan, Y. L., Wang, H. N., He, H., & Zhu, X. S. 2011, ApJ, 737, 39

Guo, Y., Ding, M. D., Wiegelmann, T., & Li, H. 2008, ApJ, 679, 1629

Hayashi, K. 2005, ApJS, 161, 480

He, H., & Wang, H. 2008, Journal of Geophysical Research (Space Physics), 113, A05S90

Jiang, C., Feng, X., Fan, Y., & Xiang, C. 2011, ApJ, 727, 101

Lites, B. W., Elmore, D. F., Seagraves, P., & Skumanich, A. P. 1993, ApJ, 418, 928

Low, B. C., & Lou, Y. Q. 1990, ApJ, 352, 343

McClymont, A. N., & Mikic, Z. 1994, ApJ, 422, 899

Metcalf, T. R. 1994, Sol. Phys., 155, 235

Metcalf, T. R., Leka, K. D., Barnes, G., et al. 2006, Sol. Phys., 237, 267

Mikic, Z., Schnack, D. D., & van Hoven, G. 1990, ApJ, 361, 690

Nakagawa, Y. 1981a, ApJ, 247, 707

Nakagawa, Y. 1981b, ApJ, 247, 719

Nakagawa, Y., Hu, Y. Q., & Wu, S. T. 1987, A&A, 179, 354

Régnier, S., & Amari, T. 2004, A&A, 425, 345

Roumeliotis, G. 1996, ApJ, 473, 1095

Schrijver, C. J., De Rosa, M. L., Metcalf, T., et al. 2008, ApJ, 675, 1637

Tóth, G. 1996, Astrophysical Letters and Communications, 34, 245

Valori, G., Kliem, B., & Keppens, R. 2005, A&A, 433, 335

Wang, A. H., Wu, S. T., Liu, Y., & Hathaway, D. 2008a, ApJ, 674, L57

Wang, H., Jing, J., Tan, C., Wiegelmann, T., & Kubo, M. 2008b, ApJ, 687, 658

Wheatland, M. S., Sturrock, P. A., & Roumeliotis, G. 2000, ApJ, 540, 1150

Wiegelmann, T. 2004, Sol. Phys., 219, 87

Wu, S. T., Wang, A. H., Liu, Y., & Hoeksema, J. T. 2006, ApJ, 652, 800

Yan, Y., & Sakurai, T. 2000, Sol. Phys., 195, 89